Liquid-liquid displacement in slippery liquid-infused membranes (SLIMs)

Hanieh Bazyar,[a,c] Pengyu Lv,[b] Jeffery A. Wood,[a] Slawomir Porada,[a,c] Detlef Lohse,[b] and Rob G. H. Lammertink,[*a]

[a] Department of science and technology, Soft Matter, Fluidics and Interfaces (SFI), University of Twente, Enschede, The Netherlands.
[b] Department of science and technology, Physics of Fluids (POF), Max Planck - University of Twente Center for Complex Fluid Dynamics, University of Twente, Enschede, The Netherlands.
[c] Wetsus, European centre of excellence for sustainable water technology, Leeuwarden, The Netherlands.
[*] Correspondence to: r.g.h.lammertink@utwente.nl

Supporting Information (SI)

SLIM fabrication and characterization

The SLIMs are fabricated by infusing Polyvinylidene fluoride (PVDF) membranes with different types of infusion liquids (hydrocarbon as well as fluorinated). Table S1 shows the physical properties of the used liquids. The pendant drop method is used to measure surface tension values using a contact angle Goniometer (Dataphysics OCA20). A modular compact Rheometer (Anton Paar MCR502) is used for measuring absolute viscosity values of the liquids, using a cone plate geometry (CP25-2). The density is measured using gas pycnometer (AccuPyc II 1340 Pycnometer) at 24 °C. (In all tables the standard deviation is reported for 6 measurements except for density which is reported for 30 measurements). The membrane is further characterized using a scanning electron microscopy (SEM) (JEOL 5600 LV), capillary flow porometer (Porolux-1000), and contact angle Goniometer (Dataphysics OCA 20).

The SEM images of top, bottom and cross section of the PVDF membrane are shown in Figure S1. The pore size distribution of the membrane is obtained from capillary flow porometry. In this measurement, nitrogen gas is pushing through the infused membrane with a low surface tension liquid, i.e. FC-43 (Table S1) at different pressures, the gas flow rate is measured correspondingly. The capillary flow porometry result for the PVDF membrane is shown in Figure S2. This measurement is conducted in two runs: in the first run, the so called wet curve, a sudden increase in gas flow rate is observed which corresponds to the pressure where the biggest pores are opened (first bubble point (FBP)). In the second run as the liquid has been already push out, a linear behaviour between flow and pressure is obtained (dry curve). The point where wet and dry curves meet corresponds to the smallest pore sizes. Simultaneously half-dry curve is also plotted where the flow values are half of the flow values of the dry curve. The crossing point of this curve and wet curve determines the mean flow pore sizes (MFP). The Young-Laplace equation (equation 1 in the paper) by considering total wetting is used to relate pressure to the pore size. Based on the results of this measurement, the pore size distribution of the membrane can be obtained which is shown in Figure S3. As can be seen from Figures S2 and S3, the PVDF membrane has a narrow and homogeneous pore size distribution with average pore radius of 1.65 μm and size distribution of 0.11 μm.

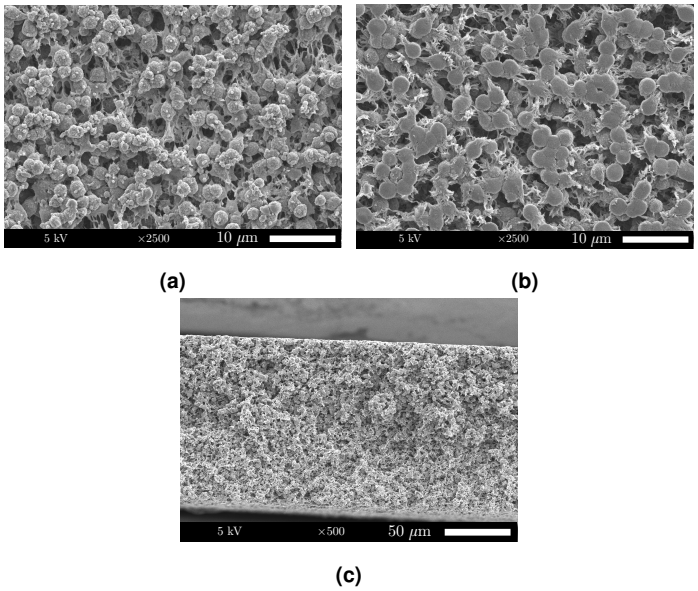

Fig. S1 Scanning electron microscopy (SEM) images of PVDF membrane. (a) Top surface, (b) Bottom surface, (c) Cross section.

Contact angle measurements

The water contact angle measurement results on dry and liquid infused PVDF membranes as well as dense PVDF are shown in table S2. The static contact angle on surfaces was measured by using drops having a volume of 2 μl. Advancing and receding contact angles were determined by placing the needle in the drop (sessile drop needle-in mode) and continuously supplying or withdrawing water up to 6 μl at 0.5 μl/min within six cycles. The delay time between each advancing and receding measurement was set to be 2 s. A high contact angle and low contact angle hysteresis are obtained for liquid infused membranes. This is the key design parameter for droplet mobility and slippery behavior of these membranes [1,2].

Table S1 Physical properties of different infusion liquids

Infusion liquids	Chemical structure	Surface tension $[mN/m]$	Absolute viscosity at 20°C $[mPa\ s]$	Kinematic viscosity at 20°C $[mm^2/s]$	Density at 24°C $[g/cm^{-3}]$
Fluorinert FC-43	Perfluorocarbon (PFC)	16.3±0.05	5.6±0.08	3.0	1.88±0.01
Galpore	Perfluoropolyether (PFPE)	15.5±0.05	8.6±0.08	4.8	1.83±0.005
Krytox GPL oil 101	Perfluoropolyether (PFPE)	16.3±0.13	25±0.1	13.5	1.85±0.01
Silicone oil AR20	Polyphenylmethylsiloxane	21.8±0.03	19.6±0.1	19.4	1.003±0.0016

Table S2 Water contact angle measurements (CA) on dry, liquid infused and dense PVDF.

Infusion liquids	Advancing contact angle (θ_{Adv}) [°]	Receding contact angle (θ_{Rec}) [°]	Hysteresis [°]	Mean static CA [°]
None (porous PVDF)	142±0.3	117±1.2	25±1	136±0.3
None (dense PVDF)	122±0.9	90±0.4	32±0.3	120±0.8
Dense PVDF immersed in Krytox 101	175±0.5	154±0.6	20±0.2	170±0.5
Dense PVDF immersed in SO AR20	161±0.4	158±0.3	2±0.4	159±0.6
Krytox 101	119±0.1	114±0.3	5.1±0.3	117±0.1
FC-43	118±0	113±0.3	4.7±0.3	116±0.3
Galpore	120±0.2	114±0.5	6.2±0.7	117±0.5
SO AR20	94±0.1	90±0.2	4.1±0.2	93±0.3

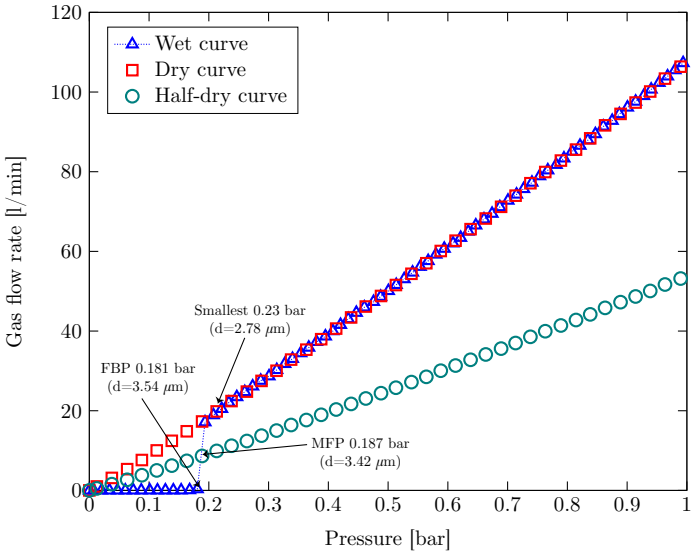

Fig. S2 Capillary flow porometry results of PVDF membrane showing flow rate of nitrogen gas as a function of pressure. The corresponding pressure values for the biggest pore sizes (first bubble point (FBP)), mean flow pore sizes (MFP) and smallest pore sizes are indicated with arrows.

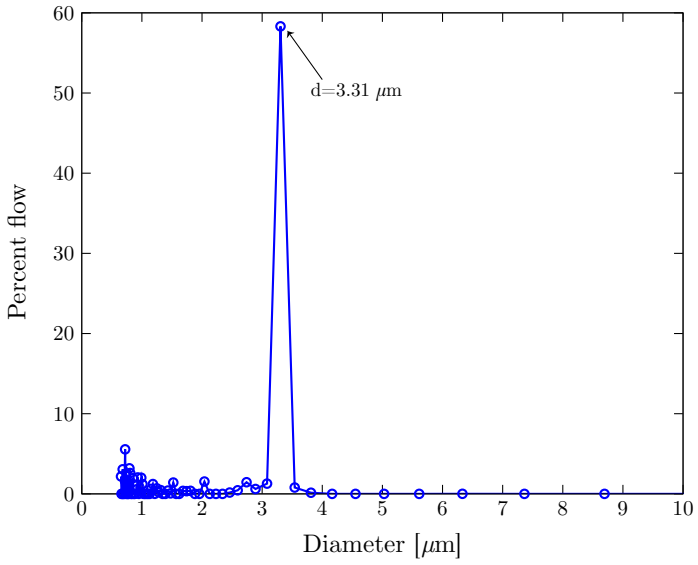

Fig. S3 Pore size distribution of the PVDF membrane.

Table S3 Interfacial tension values between water and different fluids

Fluids	Interfacial tension $[mN/m]$
Air	72.2±0.07
K101	54.7±0.16
FC-43	53.6±0.10
Galpore	53.2±0.15
SO AR20	18

Interfacial tension measurements

The surface tension of water and the interfacial tension between water and the infusion liquids are measured using a contact angle Goniometer (Dataphysics OCA 20). The pendant drop method is used for this measurement. The results are shown in Table S3. It is worth mentioning that the interfacial tension between water and silicone oil AR20 (SO AR20) could not be measured by this method, because of the very similar densities for these two liquids. Therefore, the interfacial tension between water and SO AR20 is calculated using Van der Waals components of silicone oil surface tension (which is about 18.8 mN/m)[3].

Liquid-liquid displacement porometry (LLDP) experiments

The LLDP results of infused PVDF membranes with other infusion liquids, i.e. FC-43, Galpore and SO AR20, are shown in Figure S4. Unlike other liquid infused membranes, a non-linear relation between pressure and flux is observed for SO AR20 infused mem-

brane in the 2nd run of all cycles (Figure S4(c)). The reason can be attributed to the higher kinematic viscosity of silicone oil compared to the other liquids (Table S1), resulting in slower fluid movement and thicker liquid lining on the pore wall. This will subsequently give rise to the change of pore radius with pressure [1]. Additionally, the lower pressure values for SO AR20 infused membrane compared to the other of liquid infused membranes is a direct result of the lower interfacial tension value between water and silicone oil compared to the other liquid pairs (see table S3).

Fitting results

The corresponding range of 95% confidence interval (CI) for all the fitting parameters, i.e., total number of pores per unit area N, geometric mean radius R, and geometric standard deviation S is shown in Table S4. The fitting parameters for dry and K101-infused membranes fall on the same parameter space, however, a deviation can be observed for SO AR20-infused membrane. The reason can be related to the adsorption phenomena of some unknown additives in silicone oil. LLDP experiment of SO AR20-infused membrane also shows a different behaviour compared to the other liquid-infused membranes (see Figure S4).

Relation between permeability and porosity (tube model)

Flow through a straight circular tube can be obtained from the Hagen-Poiseuille equation (equation 1) [4,5].

$$Q = \frac{\pi r^4}{8\mu}\,\frac{\Delta P}{L} \tag{1}$$

where Q is the volumetric flow rate (m^3/s), r is the radius of the tube (m), μ is the viscosity of the permeating fluid (Pa s), ΔP is the pressure drop (Pa) over the length of tube L (m). By assuming a collection of such tubes passing through a cubical piece of porous medium of length L, a simple model for permeability of the porous medium can be derived. If we have n tubes of length L and radius r, passing directly through the sample at right angles to one pair of faces, then the porosity ϕ will be given by equation 2.

$$\phi = \frac{n\pi r^2}{L^2} \tag{2}$$

The total volumetric flow through the medium is given by $Q_{total} = nQ$ (equation 3), where Q is obtained from equation 1.

$$Q = \frac{\phi L^2 r^2}{8\mu}\,\frac{\Delta P}{L} \tag{3}$$

Comparison of equation 3 with Darcy's law (equation 4) [6] gives us equation 5 for the permeability of this simple one-dimensional model.

$$Q = \frac{\kappa A}{\mu}\,\frac{\Delta P}{L} \tag{4}$$

$$\kappa = \frac{\phi r^2}{8} \tag{5}$$

A pseudo three-dimensional tube model can be obtained by arranging the n capillaries in such a way that $n/3$ capillaries are parallel to the z-axis. In this model, the permeability for the same

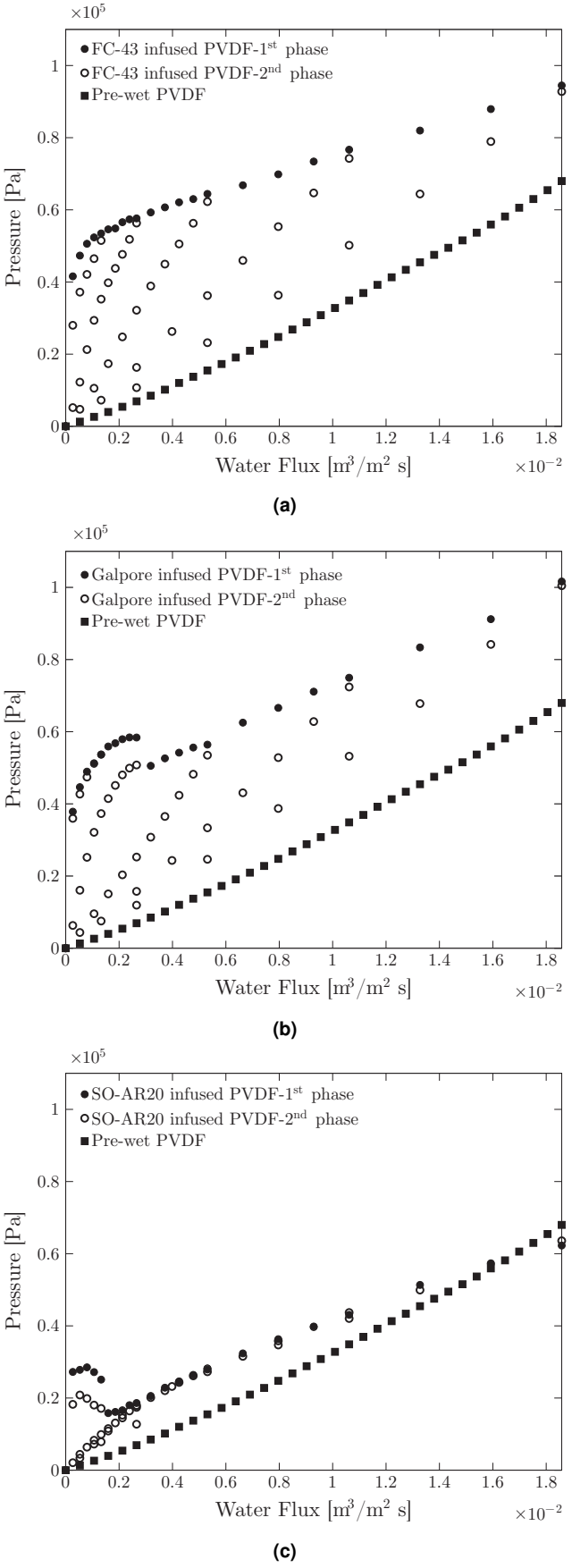

Fig. S4 Liquid-liquid displacement porometry experiments of infused PVDF membrane with (a) FC-43, (b) Galpore, and (c) SO AR20.

Table S4 Range of 95% confidence interval for all fitting parameters.

Membranes	log N	log R	S
Dry	12.09±0.86	-6.39±0.23	1.53±0.14
K101-infused	10.55±0.09	-6.07±0.03	1.37±0.03
SO AR20-infused	13.57±1.76	-7.59±0.78	2.82±0.55

porosity ϕ is one-third of the permeability of the one-dimensional model (equation 5). Therefore, the three-dimensional tube model will be derived as equation 6.

$$\kappa = \frac{\phi r^2}{24} \tag{6}$$

Fabrication of the microfluidic chip

The microfluidic chip was fabricated using standard photolithography and deep reactive ion etching (DRIE) techniques at MESA$^+$ Nanolab/clean room at the University of Twente. The process can be divided in to three steps, namely etching of the pore network into the silicon (Si) wafer, etching the access holes through the Si wafer and finally bonding the finished Si wafer to a Pyrex wafer. The photolithography was done twice using two masks to make the pore network (pillars) and the access holes respectively. Before starting the photolithography, the Si wafers were thermally oxidized to get a SiO_2 layer of 1 μm, i.e. hard mask. This was done by wet oxidation of Si wafer at temperature of 1150°C for 2 hours and 20 minutes. After coating the Si wafer with a photoresist layer, the first mask was aligned with the wafer and the pillar pattern is transferred to the layer by exposure to UV light and resist development. The developed resist layer is then annealed at temperature of 120°C for 10 minutes using a hot plate. The next step is to etch the protection SiO_2 layer and then the pillar pattern into the Si wafer (to a depth of 50 μm) using DRIE technique (Bosch process recipe was used). Then the photoresist layer was stripped using oxygen plasma and a protection foil (Dupont MX 5020 foil) was applied to the top side. By the same procedure, a positive photo resist layer was developed using the second mask on the backside of Si wafer. The access holes are etched and the photoresist and foil were stripped away. Finally, the remaining SiO_2 layer was removed by dipping the wafer in buffered HF solution (BHF (1:7)) for 20 minutes. Finally, the wafer was cleaned using piranha (H_2SO_4:H_2O_2 (3:1) vol.%) and dried. The finished Si wafer was anodically bonded to the Pyrex wafer.

Liquid-liquid displacement in microfluidic chip

The remaining infusion liquid in the chip after displacing with water can be in the form of pools, bridges and thin films around pillars (Movie S1 and still image (figure S7)). The plot of specific interfacial length between water and remaining infusion liquid (including all liquid structures) is shown in Figure S5.

The specific interfacial length (a_{it}) (mm^{-1}) is calculated as interfacial length (mm) divided by the pore area (mm^2) which is defined as the porosity times the total chip area. These lengths include interfaces between wetting and non-wetting fluids as well as thin films around pillars. In Figure S5(b) the specific interfacial length for fluid-fluid interfaces is shown. The total specific

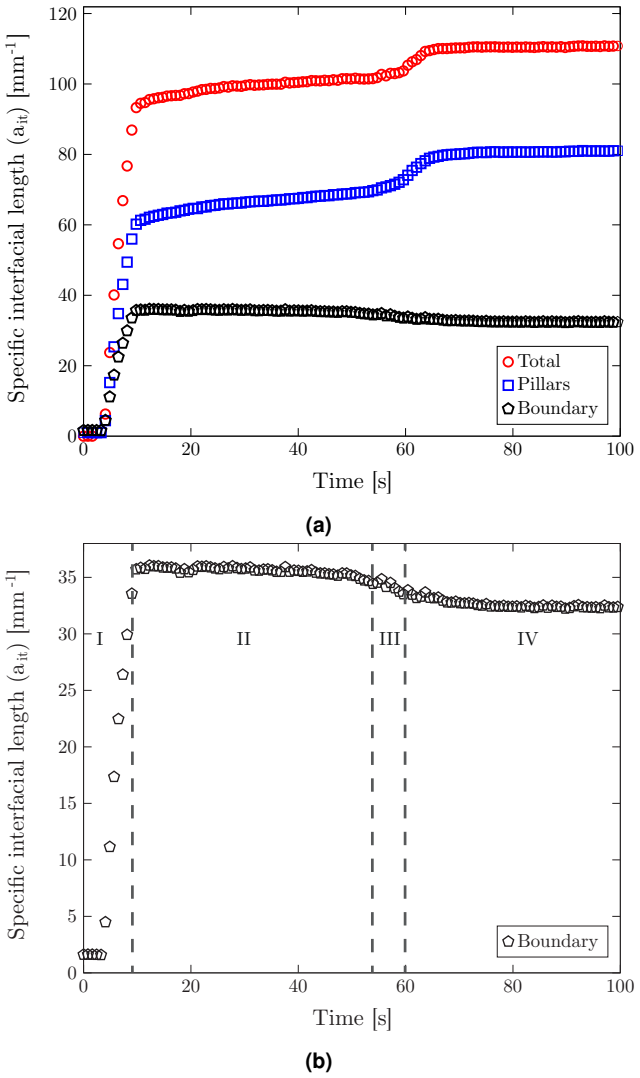

Fig. S5 (a) Specific interfacial length between water and remaining infusion liquid in the chip as a function of time. a_{it} between water and thin films around pillars is shown as squares (Pillars). a_{it} between water and other structures of the remaining infusion liquid (pools and bridges) is shown as pentagons (Boundary). The summation of these two specific interfacial lengths is shown as circles (Total). (b) Specific interfacial length (a_{it}) as a function of time for the boundary between water and oil phases.

interfacial length including thin films around pillars is shown in Figure S5(a). The observation of thin films around pillars further confirms the presence of the liquid-lined pores in the membranes. This is crucial for anti-fouling characteristics of liquid infused surfaces. A three-dimensional image of the chip is taken using a laser scanning confocal microscope (LSCM) to show the presence of this thin films along the pillars (Figure S6).

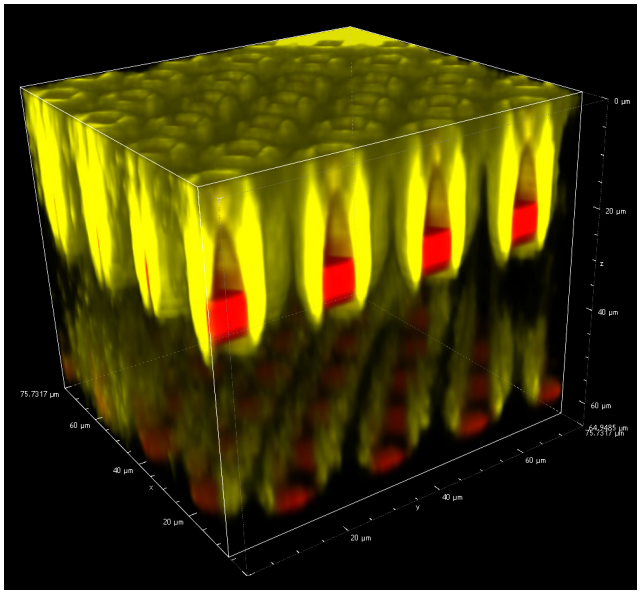

(a)

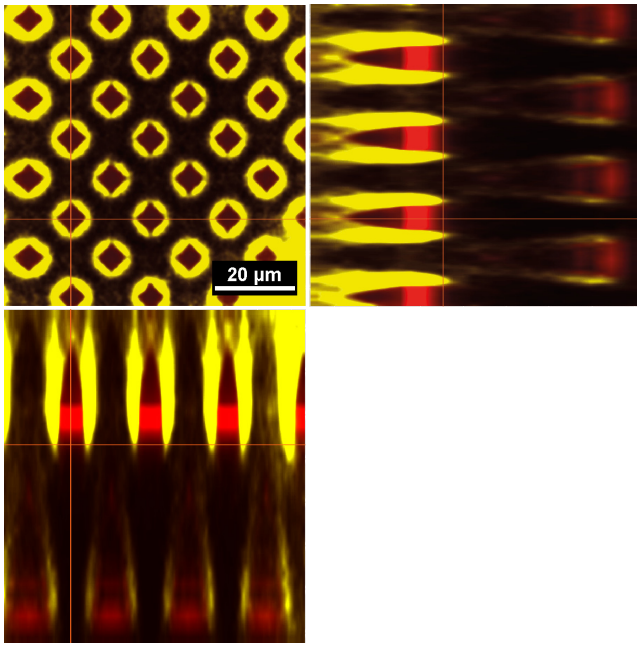

(b)

Fig. S6 (a) Three-dimensional image of the chip after displacing the infusion liquid with water (b) cross section of the three-dimensional image showing the presence of thin liquid film along the pillars (red colors are indicating pillars and yellow color shows the remaining infusion liquid (SO AR20)).

The optical sectioning resolution of 5.76 μm for z-stack imaging is used in LSCM. Due to the distortion induced by mismatch of

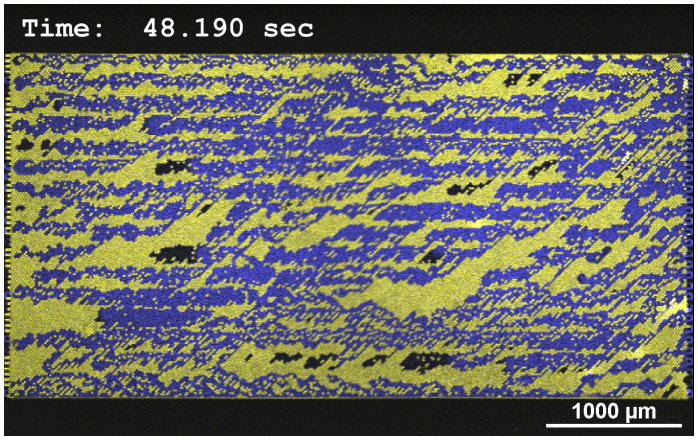

Fig. S7 Liquid-liquid displacement in the microfluidic chip. The chip is infused with oil (yellow phase) and water is pushed at flow rate of 0.2 $\mu l/s$ from the right side (blue phase).

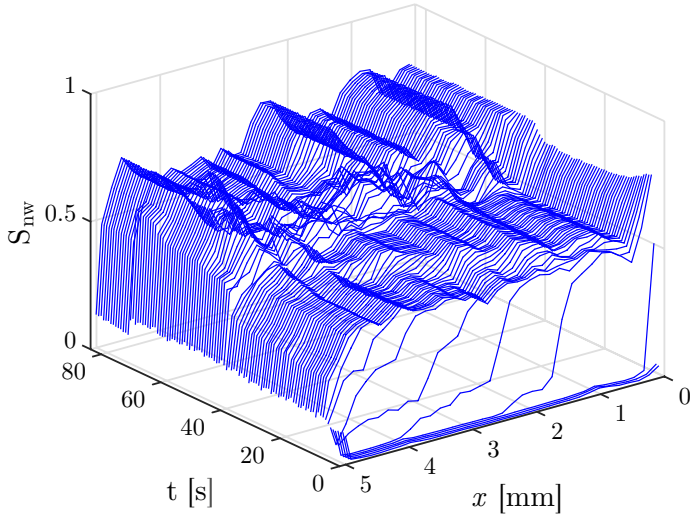

Fig. S8 Local Saturation of the non-wetting phase (S_{nw}) as a function of x and time index for the corresponding displacement movie.

the refractive index between water, glass and air the height of the pillar is observed less than 50 μm. In order to correct for that, the cross sectional images (Figure S6(b)) are re-scaled. The conical shape that is observed is because of defocusing.

Local saturation of the non-wetting phase

In order to better quantify the formation and evolution of the fingers, local saturation of non-wetting phase (S_{nw}) is plotted as a function of time (t) and location (x). For measuring the local saturation, each time frame of the displacement movie is divided vertically into 33 slices and S_{nw} is calculated for each slice. The result is shown in Figure S8, where the first four time frames show the initial formation of the fingers. This corresponds to the movement of a shock front towards the outlet.

Box counting algorithm

Hausdorff MATLAB code (Hausdorff (Box-Counting) fractal dimension code) is used for fractal dimension analysis using a box count-

ing algorithm. In the algorithm, each image is first transformed to a binary image. In this image nonzero pixels belong to an object and zero pixels constitute the background. The image is then covered by a grid and the number of grid boxes which contain at least one object pixel are counted. The same procedure will be repeated but with a finer grid with smaller boxes. D is then the slope of the line when $\log B$ (number of boxes) is plotted against $\log a$ (inverse of the box size) (see equation 7 in the main paper).

Buckley-Leverett analysis

To derive Buckley-Leverett equation, one should start with Darcy's law (or relative permeability equations) and continuity equations for each phase (wetting and non-wetting). By considering the law relating capillary pressure to saturation and concept of fractional flow (the ratio of each phase velocity to total velocity), equation 7 will be obtained for one-dimensional immiscible displacement. (For the detailed and full derivation reader is referred to reference[7]).

$$\frac{u}{\phi}\left(\frac{d\varphi_{nw}}{dS_{nw}}\frac{\partial S_{nw}}{\partial x}+\frac{\partial}{\partial x}(\psi_{nw}\frac{\partial S_{nw}}{\partial x})\right)+\frac{\partial S_{nw}}{\partial t}=0 \tag{7}$$

Where φ_{nw} and ψ_{nw} are defined as equations 8 and 9.

$$\varphi_{nw}=\frac{\frac{\mu_w}{\kappa_{rw}}+\frac{\kappa(\rho_w-\rho_{nw})g}{u}}{\frac{\mu_w}{\kappa_{r_w}}+\frac{\mu_{nw}}{\kappa_{r_{nw}}}} \tag{8}$$

$$\psi_{nw}=\frac{\kappa}{u}\frac{1}{\frac{\mu_w}{\kappa_{rw}}+\frac{\mu_{nw}}{\kappa_{rnw}}}\frac{dP_c}{dS_{nw}} \tag{9}$$

In these equations, u is the total fluid velocity (m/s), ϕ is porosity, S_{nw} is the saturation of non-wetting phase, P_c is the capillary pressure defined as difference between pressure of wetting and non-wetting phases, μ is absolute viscosity (Pa s), ρ is density (kg/m^3), κ is absolute permeability, and κ_r is relative permeability of the porous medium. The subscripts w and nw stand for wetting and non-wetting phases respectively.

Equation 7 is a parabolic partial differential equation (PDE) of unknown function S_{nw} and its partial derivatives up to the second order. If this equation can be integrated, the problem is completely solved. There are stationary solutions for this equation, but some problems of the displacement of one fluid by another having practical importance can not be solved by a stationary solution. However, since a non-stationary solution is somewhat complicated, Buckley and Leverett have considered replacing equation 7 with a simpler one by neglecting the term representing the action of capillary forces[8]. This assumption is valid when the gradient of capillary pressure ($\frac{\partial P_c}{\partial x}$) vanishes which is the case if the flow rate or fluid velocity is large and the density difference ($\rho_w-\rho_{nw}$) is small or gravity is not important. Finally, the Buckley-Leverett equation will be obtained as equation 10.

$$\frac{\phi}{u}\frac{\partial S_{nw}}{\partial t}+\frac{df_{nw}}{dS_{nw}}\frac{\partial S_{nw}}{\partial x}=0 \tag{10}$$

In equation 10, f_{nw} is the fractional flow for the non-wetting phase which is defined as equation 11.

$$f_{nw}=\varphi_{nw}+\psi_{nw}\frac{\partial S_{nw}}{\partial x} \tag{11}$$

Based on the assumption of Buckley-Leverett, P_c is virtually zero or independent of S_{nw} and saturation is a function of x which varies very slowly. In this case, $\psi_{nw}\frac{\partial S_{nw}}{\partial x}$ is small compared to φ_{nw} and $f_{nw}=\varphi_{nw}$.

Neglecting the action of capillary forces lowers the order of equation 7 by one unit gives the Buckley-Leverett equation (equation 10) as a first order PDE for the unknown function S_{nw}. To solve equation 10, the MATLAB reservoir simulation tool box (MRST) is used[9]. The solution imposes the requirement that there must be a shock front at which there is discontinuity in the function of S_{nw}.

To solve the Buckley-Leverett equation, a model is required to relate relative permeability to saturation values. We used a pure power-law relationship, the Corey model (equation 12).

$$\kappa_{rw}=(\widehat{S}_{nw})^{n_w}k_w^0, \qquad \kappa_{rnw}=(1-\widehat{S}_{nw})^{n_{nw}}k_{nw}^0 \tag{12}$$

where the exponents $n_w>1$ and $n_{nw}>1$ and the constants k_α^0, used for endpoint scaling, are fitting parameters.

$\widehat{S}_{nw}$ is the normalized non-wetting saturation defined as equation 13. The exponents n_w and n_{nw} are estimated using the Purcell model. In this model the exponents are equal to $\frac{2+\lambda}{\lambda}$ where λ is a parameter related to pore size distribution of the sample[10].

$$\widehat{S}_{nw}=\frac{S_{nw}-S_{nwr}}{1-S_{nwr}} \tag{13}$$

Here, we use a simplified version of the Corey model in which the residual saturations S_{nwr} and S_{wr} are assumed to be zero and the end points are scaled to unity, so that $\kappa_{rw}=(S_{nw})^{n_w}$ and $\kappa_{rnw}=(1-S_{nw})^{n_{nw}}$. In our model, λ is estimated as one and therefore the exponents n_w and n_{nw} are equal to three.

One more parameter which should be defined in order to solve the Buckley-Leverett equation is the absolute permeability (κ) of the porous medium. Kozeny-Carman equation (equation 14) is used to calculate this parameter for our porous micro model[11].

$$\kappa=\frac{\phi^3}{6S^2} \tag{14}$$

Equation 14 is a generalization of the tube model (6) assumes that resistance to flow arises from viscous drag along the pore walls. In this equation, S is the specific surface as the internal surface area per unit bulk volume (equation 15).

$$S=\frac{A_{pore}}{V_{bulk}} \tag{15}$$

In equation 15, A_{pore} consists of two parts, i.e. $A_{pore_{(1)}}$ and $A_{pore_{(2)}}$. $A_{pore_{(1)}}$ is calculated from the porosity of the micro model ($\phi\times A_{chip}$) where A_{chip} is the area of the microfluidic chip. $A_{pore_{(2)}}$ is the total circumferential area of the pillars ($4ah\times n$) where a and h are the side length and height of the square pillars respectively and n is the number of pillars in the microfluidic chip (62500).

References

1 H. Bazyar, S. Javadpour and R. G. H. Lammertink, *Adv. Mater. Interfaces*, 2016, **3**, 1600025–n/a.

2 C. Semprebon, G. McHale and H. Kusumaatmaja, *Soft Matter*, 2017, **13**, 101–110.

3 M. Kobayashi, Y. Terayama, H. Yamaguchi, M. Terada, D. Murakami, K. Ishihara and A. Takahara, *Langmuir*, 2012, **28**, 7212–7222.

4 G. Hagen, *Annalen der Physik und Chemie*, 1839, **46**, 423–442.

5 J. L. Poiseuille, *Comptes rendus de l'Académie des sciences*, 1840, **11**, 961–967, 1041–1048.

6 H. Darcy, *Les Fontaines Publiques de la Ville de Dijon*, Victor Dalmont, Paris, Paris, 1856.

7 C. Marle, *Multiphase Flow in Porous Media*, Gulf Publishing Company, Houston, Texas, 1981, pp. 35–92.

8 S. E. Buckley and M. C. Leverett, *Trans. AIME*, 1942, **146**, 107–116.

9 K.-A. Lie, *An introduction to reservoir simulation using MATLAB: User guide for the Matlab Reservoir Simulation Toolbox (MRST)*, SINTEF ICT, December 2016, http://www.sintef.no/Projectweb/MRST/Publications, SINTEF ICT, Department of applied mathematics, Oslo, Norway, 2016, pp. 231–267.

10 M. Sahimi, in *Flow and Transport in Porous Media and Fractured Rock*, Wiley-VCH Verlag GmbH and Co. KGaA, Weinheim, Germany, 2011, pp. 519–573.

11 P. C. Carman, in *Flow of gases through porous media*, Academic Press, Cambridge, Massachusetts, 1956, pp. 1–18.